Wave Energy Converter Power Take-Off Modeling and Validation From Experimental Bench Tests

Simone Giorgi 🆔, Ryan G. Coe 🆔, Meagan M. Reasoner 🆔, Giorgio Bacelli 🆔, Dominic D. Forbush 🆔, Scott Jensen, François Cazenave 🆔, and Andrew Hamilton

Abstract—This article describes the implementation of a new numerical model of the power take-off system installed in the Monterey Bay Aquarium Research Institute wave energy converter, a device developed to provide power to various oceanic research missions. The simultaneous presence of hydraulic, pneumatic, and electrical subsystems in the power take-off system represents a significant challenge in forging an accurate model able to replicate the main dynamic characteristics of the system. The validation of the new numerical model is addressed by comparing simulations with the measurements obtained during a series of bench tests. Data from the bench tests show good agreement with the numerical model. The validated model provides deeper insights into the complex nonlinear dynamics of the power take-off system and will support further performance improvements in the future.

Index Terms—Bench tests, modeling, power take-off (PTO), validation, wave energy converter (WEC).

I. Introduction

THE MBARI-WEC is a small two-body point absorber wave energy converter (WEC) developed, constructed, and deployed by the Monterey Bay Aquarium Research Institute (MBARI) [1]. This WEC has been in development by MBARI for about ten years, specifically with the objective of demonstrating this technology for the purposes of powering oceanographic instrumentation. MBARI is active in autonomous underwater vehicle (AUV) development and the ultimate goal of this WEC advancement is to power fleets of AUVs in remote locations for extended ocean process studies.

The MBARI-WEC is composed of a surface buoy and a submerged heave cone, which are mechanically connected by a

Fig. 1. MBARI-WEC system diagram showing mechanical layout along with PTO location (lengths are shown in meters).

power take-off (PTO) unit, as shown in Fig. 1. The PTO system consists of hydraulic, pneumatic, and electrical subsystems. Typically, the system is deployed with the submerged heave cone anchored to the seafloor with a chain-catenary mooring and an anchor. The usual deployment location is Monterey Bay, California, and is performed in approximately 80 m of water.

An ongoing study is focused on improving predictive modeling capabilities for the WEC and potentially making changes to the design to improve performance. The previous work regarding the MBARI-WEC [1] presented two different numerical models of the full MBARI-WEC system, accounting for hydrodynamic, PTO, and mooring dynamics, where the PTO is considered as a simplified black-box model. As part of this project, a new numerical PTO model to better describe the complex nonlinear dynamics of the PTO system is being developed. The contribution of this article is the presentation of the new nonlinear, time-domain numerical model, which has been developed by taking into consideration the real physical structures of the hydraulic, pneumatic, and electric PTO subsystems. The new gray-box model of the PTO has been finalized by identifying from some specifically designed bench tests, carried out in the MBARI laboratory, some of the model parameters. Furthermore, the article includes a validation of the new numerical model by comparing the simulations with measurements obtained during a series of bench tests. These tests have been performed for each subsystem independently, as well as for the complete PTO system. The implemented PTO model, described in this work, will contribute to a better understanding of the system and new knowledge for further performance improvements.

The rest of the article is organized as follows. First, in Section II, the hydraulic, pneumatic, and electrical subsystems of the PTO system are described. Section III outlines the numerically implemented MATLAB–Simulink–Simscape model. A comparison of the bench tests and simulations is shown in Section IV. Finally, Section V concludes this article.

II. PTO System

The MBARI-WEC is a two-body system composed of a buoy at the surface and a subsurface heave cone located about 30 m below (see Fig. 1). Relative motion induced by the surface waves between the buoy and heave cone acts on the WECs PTO. The PTO system is a combination of electrical, hydraulic, and pneumatic subsystems (see Fig. 2). When in motion, the hydraulic piston drives oil through a fixed-displacement hydraulic motor, which is directly coupled to a three-phase brushless electric motor. As shown in Fig. 2, the hydraulic piston and the pneumatic air spring piston are rigidly connected together. Acting together, the hydraulic and pneumatic components can provide a damping and spring force to the system, respectively. The hydraulic, pneumatic air spring, and electrical subsystems are described in further detail in Sections II-A, II-B, and II-C, respectively.

A. PTO Hydraulic Subsystem

A fixed-volume hydraulic system serves to transmit mechanical power between the piston rod and electrical motor/generator. The main components of this hydraulic subsystem are the hydraulic piston, relief valve, and hydraulic motor (see Fig. 2). The double-acting hydraulic ram has a piston rod on both sides, which results in an equal annular area of 8.87e-4 m² on both sides of the piston. The total piston stroke is equal to 2.03 m (see
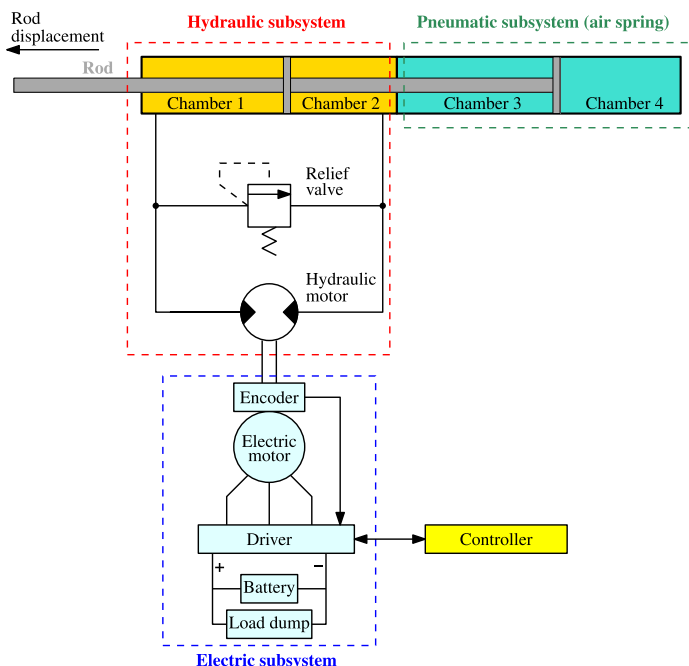
Fig. 2.   MBARI-WEC PTO system divided into hydraulic, pneumatic air spring, and electrical subsystems.

TABLE I
Hydraulic and Pneumatic Cylinder Characteristics

Parameter	Value
Total stroke	2.03 m
Hydraulic piston annular area chamber 1 (A_1)	8.87e-4 m²
Hydraulic piston annular area chamber 2 (A_2)	8.87e-4 m²
Piston rod total mass (M)	48 kg
Air spring piston area chamber 3 (A_3)	115.2e-4 m²
Air spring piston area chamber 4 (A_4)	126.7e-4 m²
Air spring dead volume chamber 3	0.0523 m³
Air spring dead volume chamber 4	0.0267 m³

Table I). In this article, these two hydraulic piston chambers are called 1 and 2 (see Fig. 2).

The piston converts the heave motion of the buoy into a pressurized, bidirectional fluid flow, and the hydraulic motor converts the hydraulic fluid flow and pressure into rotational motion and torque. The shaft of the hydraulic motor is connected directly (no gearboxes are utilized) to the electric motor shaft, causing it to spin and generate electricity. Since there is no hydraulic rectification, the hydraulic and electric motors reverse rotary direction with a change in piston direction of motion. The hydraulic motor is a Parker F11-5 model, which is a bent axis (40° angle between shaft and cylinder barrel) fixed displacement motor (see key parameters in Table II). The mechanical, volumetric, and total efficiency values are provided by the manufacturer in tabulated form and are shown in Fig. 3. The pressure relief valve shown in Fig. 2 is a critical safety component in

This article has been accepted for inclusion in a future issue of this journal. Content is final as presented, with the exception of pagination.

GIORGI et al.: WEC PTO MODELING AND VALIDATION FROM EXPERIMENTAL BENCH TESTS

3

TABLE II
HYDRAULIC MOTOR CHARACTERISTICS (PARKER F11-5)

Parameter	Value
Displacement (D)	4.9 cm^3/rev
Max continuous pressure	350 bar
Max continuous speed	10800 R/min
Max continuous input flow	52 l/min
Moment of inertia	0.16e-3 kg m^2
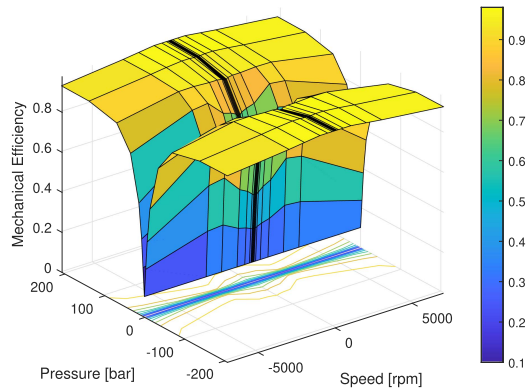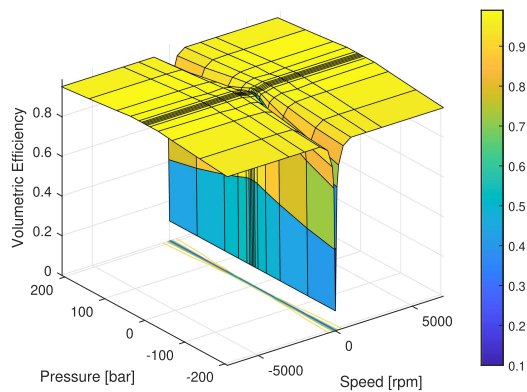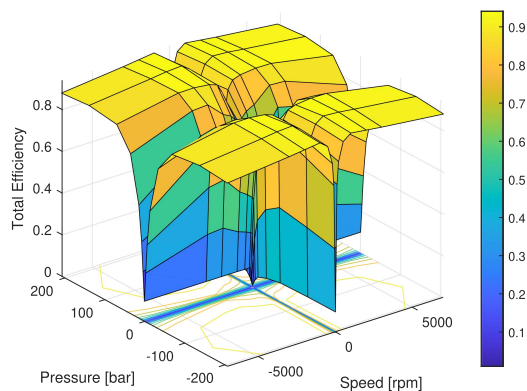
TABLE III
ELECTRIC MOTOR KOLLMORGEN AKM63S CHARACTERISTICS (PROVIDED BY
THE MANUFACTURER)

Parameter	Value
Stator winding	3 coils, star connection
Pole pairs	5
Back EMF	Sinusoidal
Coulomb friction (τ_c)	0.1 N·m
Moment of inertia	2.42e-3 kg m^2
Viscous coefficient (k_v)	0.06 N·m/(kr/min)
Torque constant (k_t)	0.62 ± 10% N·m/A$_{rms}$

the system that prevents an overspeed condition of the hydraulic and electric motors. To achieve this, the control electronics exert maximum back-pressure on rod extension as the rotor speed exceeds 5500 r/min, guaranteeing the pressure relief valve (set at 200 bar) will open and reduce the oil flow through the hydraulic motor no matter how hard and fast the ocean waves pull the hydraulic ram.

B. Pneumatic Air Spring Subsystem

An air spring assembled in line with the hydraulic piston (see Fig. 4) is employed to accommodate the weight of the heave cone and maintain a taught connection between the buoy and heave cone. The air spring device is a pneumatic piston containing nitrogen gas in both piston chambers, having the rod only on one side of the piston head, which results in two different effective areas for chambers 3 and 4 (see Fig. 2 and Table I). The hydraulic and pneumatic pistons are rigidly connected together (the hydraulic and air spring subsystems have the same rod with a total moving mass of 48 kg). On both sides of the piston, a dead volume is present (see Table I). Apart from leakage across the piston that occurs at a very slow rate (days to weeks for a measurable change to occur), no mass flow occurs between chambers 3 and 4. As a first-order approximation, the restoring force provided by the air spring is about 8.9 kN when the rod extension is 1 m.

C. PTO Electrical Subsystem

As shown in Fig. 2, a Kollmorgen AKM63S brushless motor serves as the motor/generator in the system. This is a three-phase permanent magnet motor with a maximum continuous current rating of 35 A (see motor characteristics in Table III). Electrical machines such as this are characterized by a linear relationship between the winding current $I_w^{(rms)}$ and the generated electromagnetic torque τ_e

$$\tau_e = k_t I_w^{(rms)} \tag{1}$$

where k_t is the torque constant, having a value (provided by the manufacturer) shown in Table III.

The three-phase motor windings are connected to a 10-kW (peak) 4-quadrant custom motor drive, which controls the motor

Fig. 3. Hydraulic motor efficiency surfaces. (a) Mechanical efficiency. (b) Volumetric efficiency. (c) Total efficiency. Surface colors correlate with vertical axes.
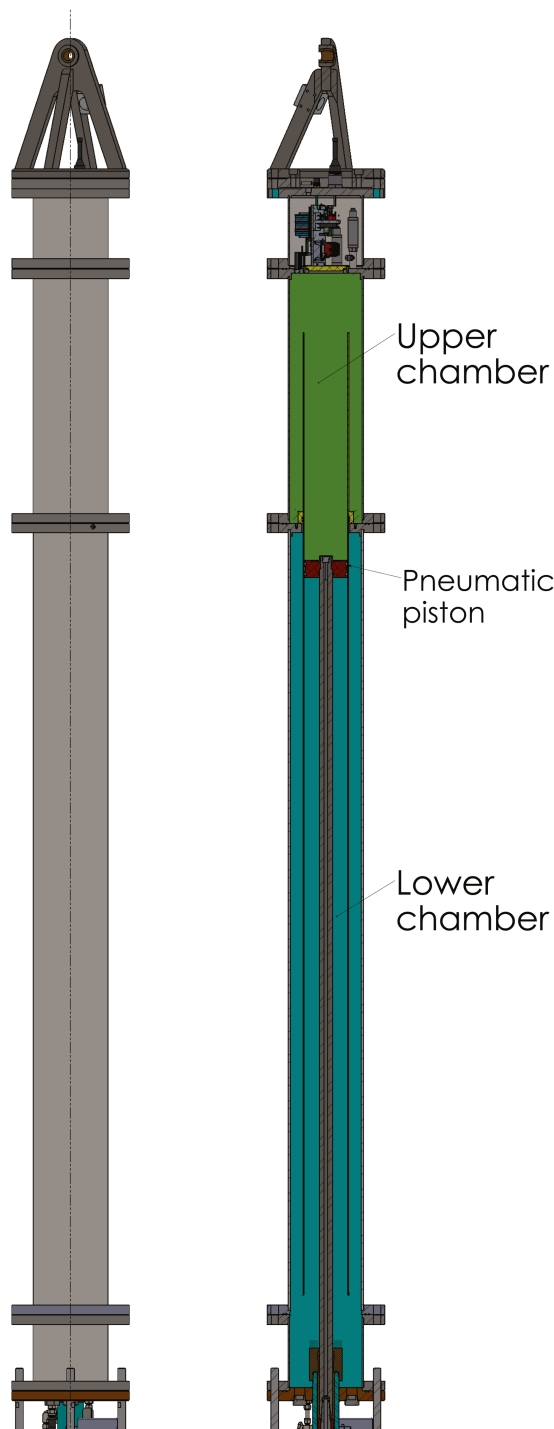
Fig. 4. Pneumatic spring cross-section.

winding current (and, therefore, indirectly the generated torque) to a set value by using field-oriented control techniques [2]. While these are standard techniques in the permanent magnet servo motor industry, the power electronics that implement these behaviors in the MBARI-WEC have been custom developed and are implemented on a Microchip dsPIC33F microcontroller and DSP combination. The work to develop this custom motor driver was undertaken because the wave energy application at this scale has some very specific requirements, which are hard to meet using commercially available power electronics. In particular, the

efficiency requirements of the system are important, especially at low speed because the rotor stops and changes direction with each wave. In this type of motor drive, switching losses in the transistors are a significant component of the total lost power, since these losses do not diminish at low speeds and low winding currents (such as other resistive losses in the system). For this reason, the MBARI motor driver turns OFF the transistor bridge at low speeds and torques to eliminate switching losses at these operating points.

Additional specialty features include the ability to bootstrap the system from a zero-speed and power-down condition. Because a WEC cannot be left unloaded without damage, the system needs to begin rotating and applying appropriate torques, even if the battery power to the system is not present due to depleted or disconnected batteries. Similarly, overspeed and overcurrent conditions must be safely handled should they occur, and the system needs to restart to normal operation on the next wave cycle without user intervention. All of these features and characteristics are somewhat specific to wave energy conversion and hard to achieve in commercially available motor-drive systems, which are often optimized for factory applications.

This system is a four-quadrant device that can act as a generator and convert mechanical energy to electrical energy, or as a motor in which electrical energy is converted to mechanical energy. By default, the system remains in generator mode but can be programmatically commanded to deliver any desired torque to the rotor, regardless of which torque–speed quadrant results.

When the prescribed electromagnetic torque opposes the motion of the motor, the system acts as a generator and boosts the dc bus voltage to 325 V for power transmission to the battery. In this default generation mode, the system is controlled to behave like a linear damper, in which the motor exerts a torque that is linearly proportional to the motor's rotational speed.

$$\tau_e = -k_d \omega. \tag{2}$$

Here, k_d is the damping coefficient. In practice, the system implements a default damping coefficient that can be further adjusted by a scaling factor between 0.5 and 1.4. As per (1), $I_w^{(\mathrm{rms})}$ is also linearly proportional to ω.

When operating in generation mode, if the battery cannot accept the produced power (due to being full or disconnected), the energy is directed instead to a submerged load-dump, which is part of the PTO device. This load-dump resistor has a resistance of 7.2 Ω, and the current flowing to the load dump is controlled by a pulsewidth modulation technique.

Without programmatic intervention, the system will operate in the above-described generator mode; however, it is possible to override this in the system with an arbitrary torque command that may cause the system to operate in motor mode. In the case that the commanded torque and motor rotational speed are in the same direction, the system acts as a motor and drives the shaft with a torque proportional to the winding current, drawing energy out of the battery (up to a specified current limit). In all cases, the driver controller attempts to achieve the requested torque but will self-limit in some situations for device safety considerations.

This article has been accepted for inclusion in a future issue of this journal. Content is final as presented, with the exception of pagination.

GIORGI et al.: WEC PTO MODELING AND VALIDATION FROM EXPERIMENTAL BENCH TESTS 5

III. System Modeling and Identification

The core of the PTO numerical model is an expression of Newton's second law applied to the moving piston rod.

$$M\ddot{x} = f_{\text{rod}} + f_{\text{as}} + f_{\text{hy}} + f_{\text{fric}}. \qquad (3)$$

Here, M is the total rod mass equal to 48 kg, x the rod displacement, f_{rod} the external force applied on the rod (e.g., the force applied by the WEC float/heave-cone combination or by the laboratory hydraulic test piston during the bench tests), f_{as} the air spring force, f_{hy} the hydraulic force, and f_{fric} the friction force. In (3), the positive direction corresponds to the extension direction of the piston rod (see Fig. 2). Since the piston is oriented horizontally in the laboratory, the gravitational force need not be considered. Note that when deployed at sea, the PTO is oriented vertically, therefore, necessitating the addition of a gravitational force in (3). This does not invalidate the lab tests as the performance of the device depends on the piston position and velocity only.

The hydraulic force f_{hy} can be described as a function of p_1 and p_2, respectively, the oil pressure in chambers 1 and 2

$$f_{\text{hy}} = A_2 p_2 - A_1 p_1 \qquad (4)$$

where p_1 and p_2 are numerically calculated from the interaction of the hydraulic and electrical subsystems (as shown in Fig. 2), which are described in Sections III-A and III-D, respectively. See Table I for numerical values of A_1 and A_2.

Similarly, the pneumatic force f_{as} can be determined from p_3 and p_4, the nitrogen pressure in chambers 3 and 4

$$f_{\text{as}} = A_4 p_4 - A_3 p_3 \qquad (5)$$

where p_3 and p_4 are calculated from the thermodynamic model of the air spring, explained in Section III-B (see Table I for numerical values of A_3 and A_4).

The friction force f_{fric} is evaluated from the hydraulic–pneumatic rod friction model, described in Section III-C. The model described by (3) utilizes the rod displacement and velocity (x and $\dot{x}$) along with a specified electric-motor torque as inputs, and the total force applied to the rod f_{rod} is the output. This arrangement allows straightforward integration into a simulation that includes the buoy and heave-cone dynamics and interactions with the environment, although that simulation is not included in this article.

The numerical model has been implemented using MATLAB–Simulink–Simscape software package and libraries. In particular, the Simscape software provides block libraries and special simulation tools for modeling physical systems. The model developed here relies on calibration from lab tests performed on the deployed hardware to determine various coefficients that are used to characterize the physical behavior of the systems. Sections III-A–III-D describe each subsystem model and the tests used to characterize these models.

A. Hydraulic PTO Subsystem Model

The hydraulic subsystem is modeled assuming the hydraulic oil is incompressible and isothermal; therefore, no fluid bulk modulus or thermodynamic effects are taken into account in this
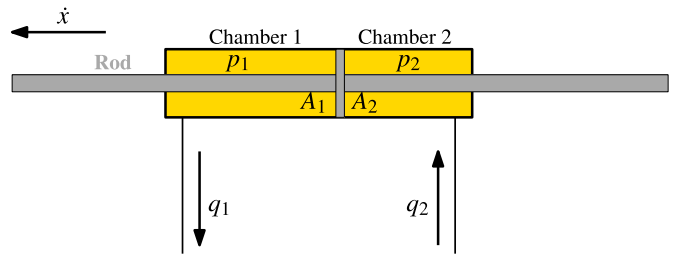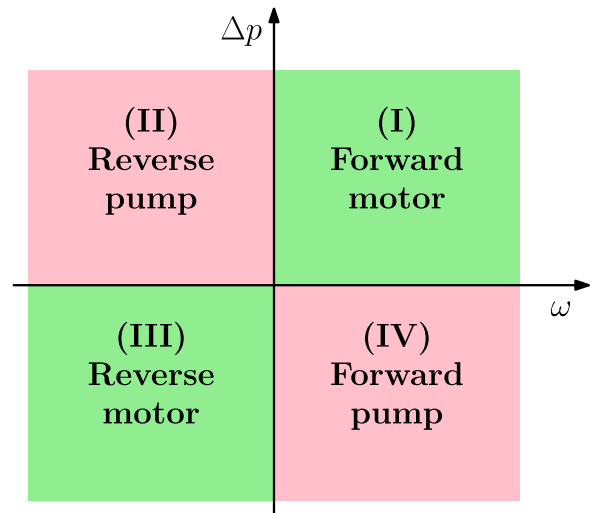

Fig. 5. Hydraulic cylinder block diagram.

Fig. 6. Hydraulic motor/pump working plane.

model. The double-acting hydraulic cylinder model is based on (4) and the following equation [3]:

$$q_i = A_i \dot{x} \qquad (6)$$

where the subscript i assumes the value 1 or 2 (meaning chamber 1 or 2), q_i is the chamber flow rate with direction convention shown in Fig. 5 and the numerical values of A_1 and A_2 are shown in Table I. The model assumes that the mechanical components are rigid with no deformations and that leakage flows are negligible. Furthermore, the friction between moving parts is not taken into account in the model of the double-acting hydraulic cylinder. Instead, the friction effect is evaluated specifically by the friction model described in Section III-C.

The hydraulic motor is modeled as a constant volumetric displacement motor, able to operate in both forward and reverse directions depending on the rotation of the shaft. This component is able to extract or provide energy to the oil (working either as a motor or a pump), depending on the differential pressure applied across the device ports Δp and on the shaft rotational speed ω. Fig. 6 shows the four quadrant operations, where in quadrants I and III, the component works as a motor (Δp and ω have the same sign), and in quadrants II and IV, the component works as a pump (Δp and ω have opposite sign).

Fig. 7 shows the model structure utilized for the hydraulic motor. For an ideal hydraulic motor, the volumetric flow q_{id} and
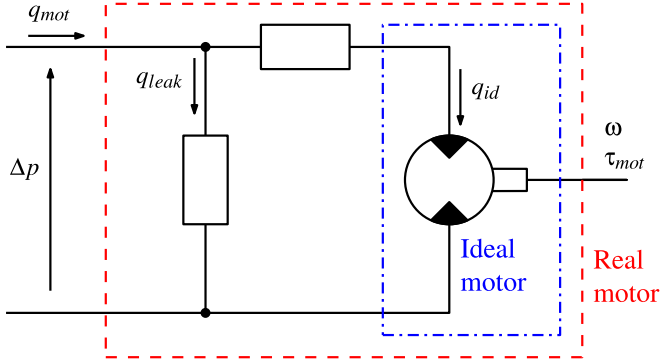
This article has been accepted for inclusion in a future issue of this journal. Content is final as presented, with the exception of pagination.

6   IEEE JOURNAL OF OCEANIC ENGINEERING

Fig. 7.   Hydraulic motor model structure.

the shaft torque τ_{id} are given by

$$q_{\mathrm{id}} = D\omega \tag{7a}$$

$$\tau_{\mathrm{id}} = D\Delta p \tag{7b}$$

where ω is the motor shaft speed, D is the cubic displacement per radian of shaft rotation, and Δp is the differential pressure applied across the motor ports.

Energy losses due to leakage flow and friction torque, present in any real hydraulic motor, are introduced into the model through the internal leakage volumetric flow rate q_{leak} and the hydraulic motor friction torque $\tau_{\mathrm{fr}}^{(\mathrm{hm})}$

$$q_{\mathrm{mot}} = q_{\mathrm{id}} + q_{\mathrm{leak}} \tag{8a}$$

$$\tau_{\mathrm{mot}} = \tau_{\mathrm{id}} + \tau_{\mathrm{fr}}^{(\mathrm{hm})} \tag{8b}$$

where q_{mot} is the net volumetric flow rate and τ_{mot} is the net hydraulic motor torque. In particular, q_{leak} and $\tau_{\mathrm{fr}}^{(\mathrm{hm})}$ are computed by using tabulated values of the volumetric efficiency η_v and mechanical efficiency η_m, which are defined as [4], [5], [6]

$$\eta_v = \frac{q_{\mathrm{id}}}{q_{\mathrm{mot}}} = \frac{D\omega}{q_{\mathrm{mot}}} \tag{9a}$$

$$\eta_m = \frac{\tau_{\mathrm{mot}}}{\tau_{\mathrm{id}}} = \frac{\tau_{\mathrm{mot}}}{D\Delta p}. \tag{9b}$$

Both η_v and η_m vary with Δp and ω, as evident in the tabulated values provided by the motor manufacturer and shown in Fig. 3.

The relief valve has been modeled as an ideal component, which remains closed when the differential pressure between inlet and outlet ports is less than the preset pressure (equal to 200 bar in this system). When the differential pressure reaches the preset pressure, the valve opens and the differential pressure between inlet and outlet ports is stabilized at 200 bar. Note that in the simulations presented in this article, the relief valve never opens, since the differential pressure is persistently less than 200 bar.

B. Pneumatic (Air Spring) Subsystem Model

The air spring model is intended to replicate the main characteristics of the real system with minimum complexity and computation costs. In particular, the model must capture the presence
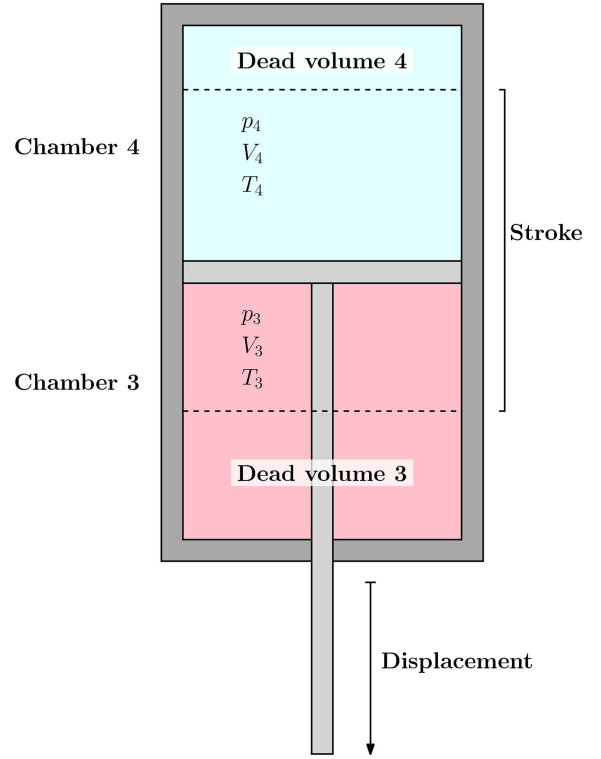

Fig. 8.   Air spring simplified geometrical model.

of a hysteresis effect between the rod displacement/velocity and pneumatic force. This hysteresis can be attributed to the presence of heat exchange between the piston nitrogen chambers and the surroundings [7] and, therefore, depends upon the speed at which the piston moves.

The complex geometry of the air spring subsystem (see Section II-B, Fig. 4) is modeled as a simplified double-acting piston (see Fig. 8), having physical parameters shown in Table I. It is assumed that the piston casing is perfectly rigid and the moving interface is perfectly sealed (i.e., each chamber is a closed system with no material exchange with the surroundings). Furthermore, the gas pressure and temperature are assumed homogeneous in each chamber, and no friction between the rod and the cylinder is introduced into the air spring model (a separate friction model accounts for the air spring friction, as explained in Section III-C). The nitrogen is modeled as an ideal gas, obeying the equation of state [8], [9]

$$pV = nRT \tag{10}$$

where p is the pressure, T the absolute temperature, V the volume, and $R = 0.2968 \, \mathrm{kJ/(kg\ K)}$ the nitrogen gas constant [8]. In each chamber, the gas pressure, volume, and temperature evolve based on (10) and on the energy balance equation (first law of thermodynamics) for a closed system [8], [9]

$$\Delta U = Q - W. \tag{11}$$

Here, ΔU is the variation of the internal energy of a closed system (for an ideal gas, the internal energy is only a function of temperature), Q the amount of energy supplied to the system in the form of heat, and W the work done by the system on its

This article has been accepted for inclusion in a future issue of this journal. Content is final as presented, with the exception of pagination.

GIORGI et al.: WEC PTO MODELING AND VALIDATION FROM EXPERIMENTAL BENCH TESTS   7
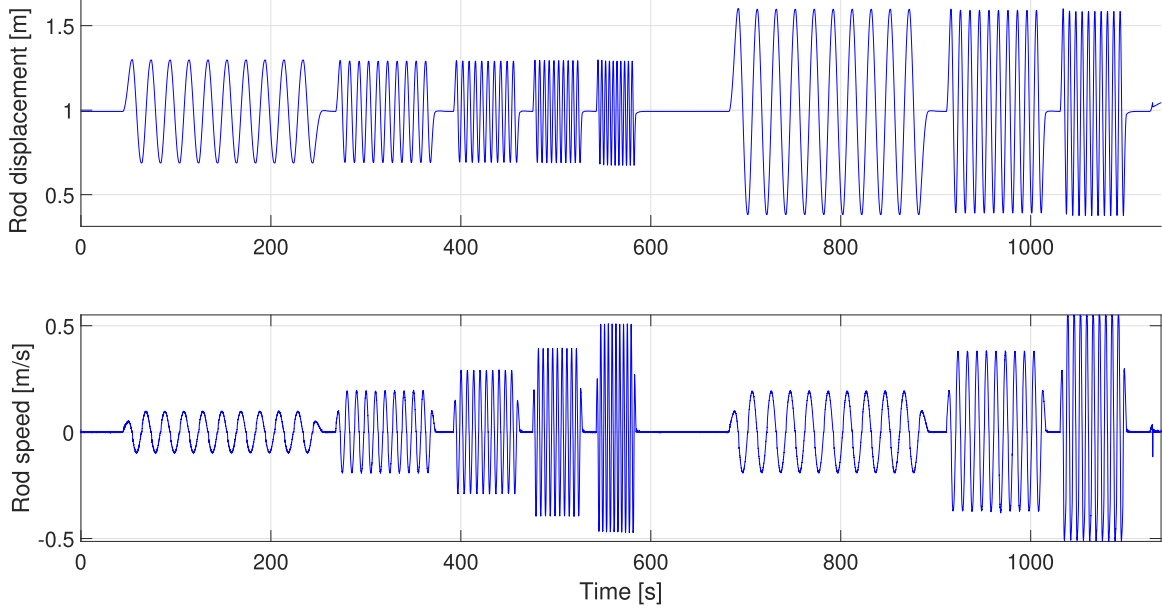

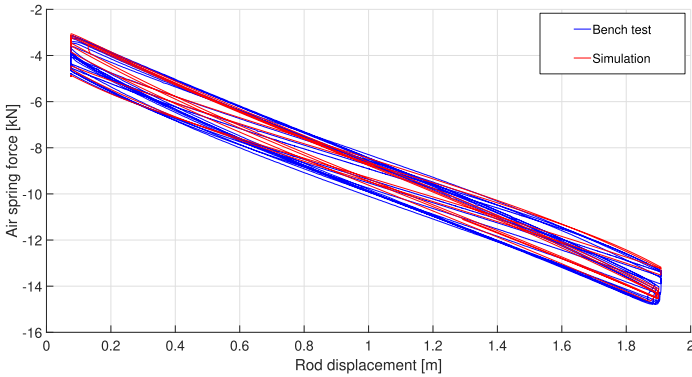Fig. 9.   Rod displacement and speed during a constant velocity bench test.

Fig. 10.   Comparison of pneumatic spring simulation and test data illustrating the hysteresis effect represented on the displacement–force plane.
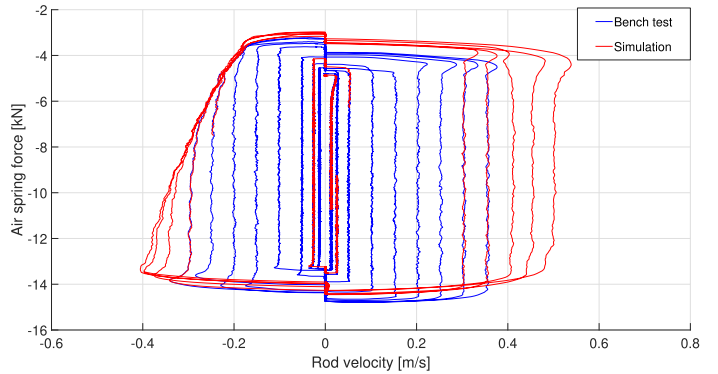

Fig. 11.   Comparison of pneumatic spring simulation and test data illustrating the hysteresis effect represented on the velocity–force plane.

surroundings. Equation (11) shows that, in a closed system, the only way for the inner gas to exchange energy with the external environment is through the heat flow across the gas boundary and mechanical work (as the pressure–volume work done by the gas on the moving interface).

In the proposed simplified heat transfer model, it is assumed that each gas chamber transfers a total heat according to [8], [10]

$$\dot{Q}_i = K_i (T_{\text{amb}} - T_i) \qquad (12)$$

where the subscript i indicates chamber 3 or 4, $\dot{Q}_i$ is the rate of heat transfer, T_{amb} is the ambient temperature (assumed equal to $10\,°\text{C} = 283.15\,\text{K}$), T_i is the chamber temperature, and K_i is the heat transfer coefficient that characterizes the model.

To complete the model, the coefficients K_3 and K_4 have been identified by fitting the model to experimental data collected during lab tests, which are characterized by a sequence of constant velocity motions (see Fig. 9). Figs. 10 and 11 show the comparison of the experimental data with the simulation results

after the identification of K_3 and K_4, where a good reproduction of the hysteresis effect is observed.

C. Hydraulic–Pneumatic Rod Friction Model

As described in Section II, the hydraulic piston and the pneumatic air spring are rigidly connected together by sharing the same rod (see Fig. 2). The rod and pistons are subjected to friction forces due to relative movement between surfaces in contact; in particular, the cylinder seals are the primary contributors. In some cases, the seals in this system are asymmetric, sealing pressure in only one direction. This causes a dependence on the direction of travel that can be seen in the test data. The hydraulic–pneumatic rod friction model is based on an assumption of a nonlinear algebraic relationship between rod velocity and friction force. In particular, the total friction force is modeled as the superposition of a Coulomb friction and a linear damping [11], [12], [13]. The Coulomb friction is a constant friction contribution only dependent on the sign of the
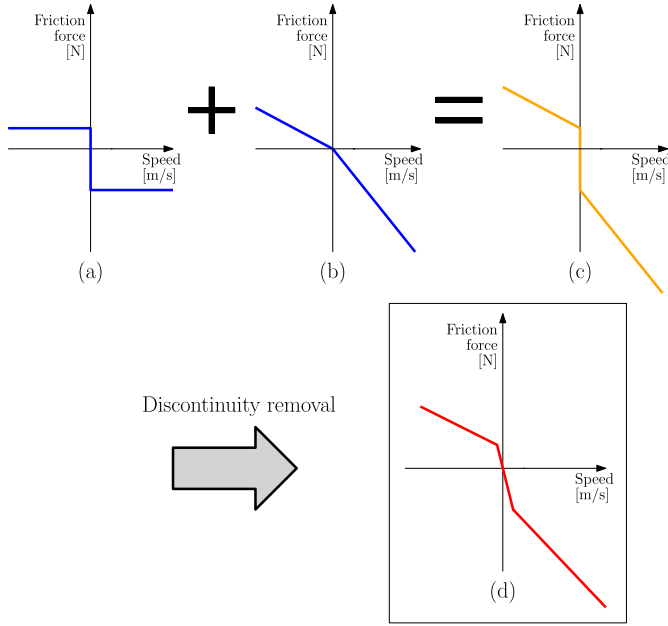
Fig. 12. Hydraulic–pneumatic rod friction model. (a) Coulomb friction force. (b) Linear viscous friction force. (c) Superposition of Coulomb and linear viscous friction force, with discontinuity around the origin. (d) Utilized friction model obtained by removing the discontinuity around the origin.

velocity (not the magnitude), as shown in Fig. 12(a). The viscous damping is assumed to be linearly proportional to the velocity [see Fig. 12(b)]. The superposition of the Coulomb friction and linear damping results in a discontinuity around the origin [see Fig. 12(c)], which represents a challenge for the numerical solutions. Therefore, the discontinuity has been removed by adding a linear connection passing through the origin, as shown in Fig. 12(d).

From (3) to (5), the friction force can be expressed as

$$f_{\text{fric}} = -f_{\text{rod}} - A_4 p_4 + A_3 p_3 - A_2 p_2 + A_1 p_1 + M\ddot{x} \quad (13)$$

which is utilized to provide an indirect measurement of the friction force from bench tests, since the time-evolution values of p_1, p_2, p_3, p_4, x, and f_{rod} are measured. In particular, the experimental data from the bench tests with constant velocity motions are used. For different velocity magnitudes and directions, it is possible to extract the constant speed value S_i and the constant friction force value F_i. The S_i and F_i values can be used to fit two distinct linear models (one model for positive speed and one model for negative speed) utilizing a least-squares methodology [14].

By carrying out a matrix of tests with different velocities and damping coefficients applied by the electric motor, five different friction models have been identified, showing a dependence of the friction model on the hydraulic loading of the system (see Fig. 13). The models shown in Fig. 13 have been averaged to obtain a single friction model applicable for all conditions.

D. Electrical Subsystem Model

The three-phase brushless motor is characterized by a linear relationship between the winding current and the generated
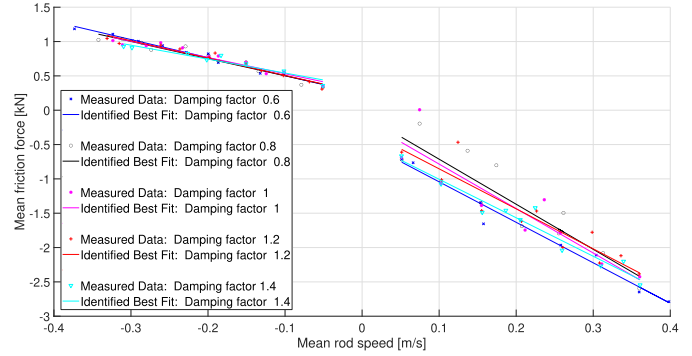

Fig. 13. Least-squares fitting to the experimental data obtained from constant speed motions. The data points used correspond only to the constant-speed portions of the tests and each curve corresponds to a different amount of hydraulic pressure during the motions. As expected, a weak dependence on hydraulic pressure is exhibited.
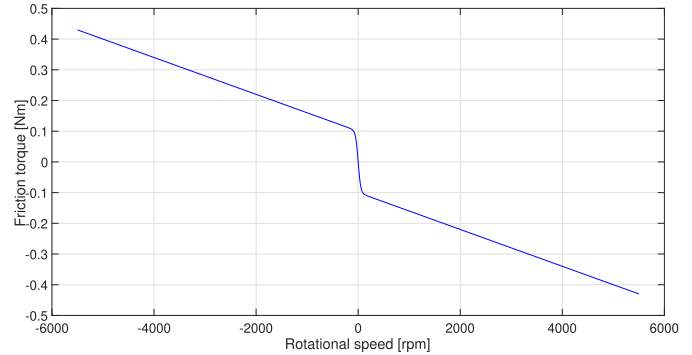

Fig. 14. Friction model implemented for the electric motor.

electromagnetic torque, as shown in (1). The friction torque present in the motor $\tau_{\text{fr}}^{(\text{em})}$ can be modeled as the superposition of the Coulomb and viscous damping (a similar approach has been used for the rod friction model in Section III-C) [2], [13]:

$$\tau_{\text{fr}}^{(\text{em})} = -[\tau_c \tanh(\omega/k_{\text{th}}) + k_v \omega] \quad (14)$$

where k_{th} determines how fast the $\tanh$ function changes from -1 to +1, τ_c is the Coulomb friction torque, and k_v the viscous coefficient (see Table III). Other models use $\text{sign}(\omega)$ instead of $\tanh(\omega/k_{\text{tanh}})$ but the model given by (14) exhibits a higher numerical stability [13]. Fig. 14 shows the algebraic relationship between $\tau_{\text{fr}}^{(\text{em})}$ and ω, described by (14).

The core of the implemented electric PTO subsystem model is represented by a Simscape-Electrical motor and driver block, representing a generic motor and driver system, which abstracts the motor, driver, and control details, allowing for fast simulation at a system level (since the electrical dynamics are much faster than those of the rest of the system).

The real motor and driver system exhibits a torque saturation effect, visible on the plane speed–torque (see Fig. 15). This effect is due to the motor–driver actively limiting the amount of current that can be drawn from the battery system. This saturation effect parameterization is inserted into the Simscape block as a set of speed data points and corresponding maximum torque values.
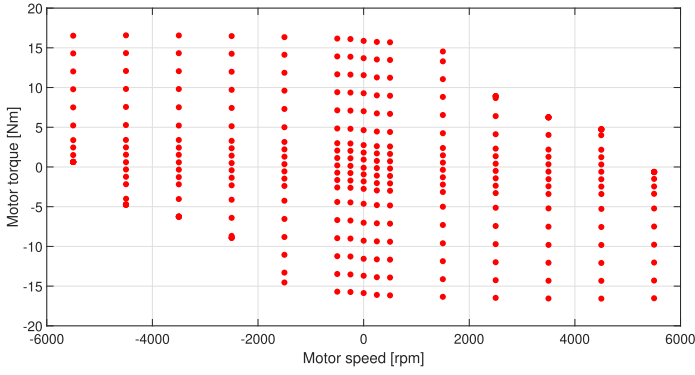
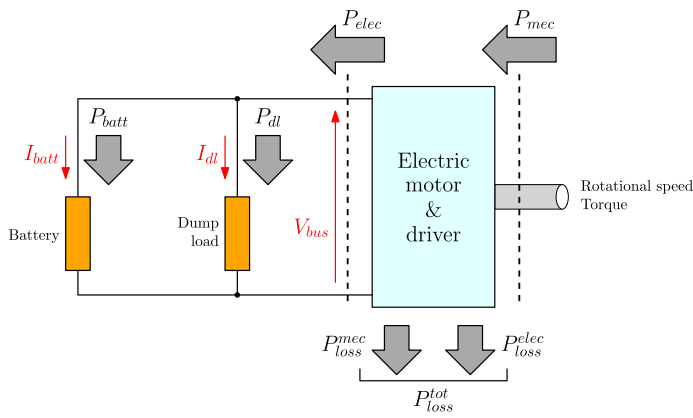Fig. 15. Electric motor test points (note operational envelope is limited by power saturation effect).

Fig. 16. Block diagram of the PTO motor and driver electrical losses.

Another fundamental characteristic of the real motor and driver system is the internal total power losses, $P_{\text{loss}}^{\text{tot}}$, which is the summation of the mechanical losses $P_{\text{loss}}^{\text{mec}}$ due to the electric motor friction force, and the electrical losses $P_{\text{loss}}^{\text{elec}}$ due to the generated heat by the electrical components

$$P_{\text{loss}}^{\text{tot}} = P_{\text{loss}}^{\text{mec}} + P_{\text{loss}}^{\text{elec}} \qquad (15)$$

where the mechanical power loss due to friction is

$$P_{\text{loss}}^{\text{mec}} = -\tau_{\text{fr}}^{(\text{em})}\omega = \tau_c \omega \tanh(\omega/k_{\text{th}}) + k_v \omega^2. \qquad (16)$$

Note the presence of the minus sign in (16), because $P_{\text{loss}}^{\text{mec}}$ is considered positive when leaving the system. The Simscape block is parameterized by providing tabulated values of $P_{\text{loss}}^{\text{elec}}$ versus motor speed and torque, which can be identified from the experimental data. Indeed, $P_{\text{loss}}^{\text{tot}}$ is the difference of the incoming mechanical power P_{mec} and the outgoing electric power P_{elec} (see Fig. 16)
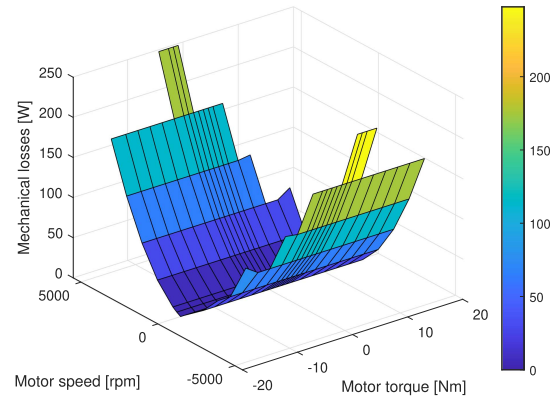
$$P_{\text{loss}}^{\text{tot}} = P_{\text{mec}} - P_{\text{elec}} = \tau_{\text{lab}}\omega - V_{\text{bus}}(I_{\text{batt}} + I_{\text{dl}}). \qquad (17)$$

Fig. 17(a) shows $P_{\text{loss}}^{\text{tot}}$ calculated with (17) from electrical subsystem tests. By combining (15)–(17), it follows that:
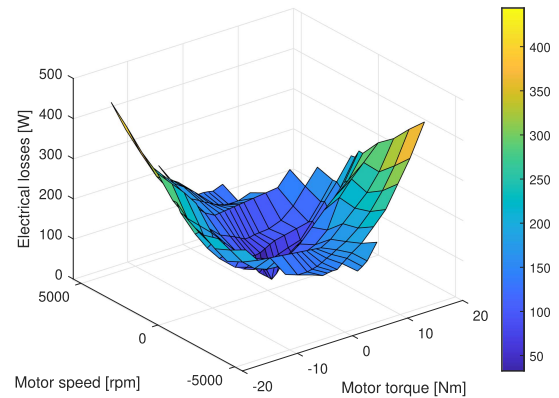
$$P_{\text{loss}}^{\text{elec}} = \tau_{\text{lab}}\omega - V_{\text{bus}}(I_{\text{batt}} + I_{\text{dl}})$$
$$- [\tau_c \omega \tanh(\omega/k_{\text{th}}) + k_v \omega^2] \qquad (18)$$
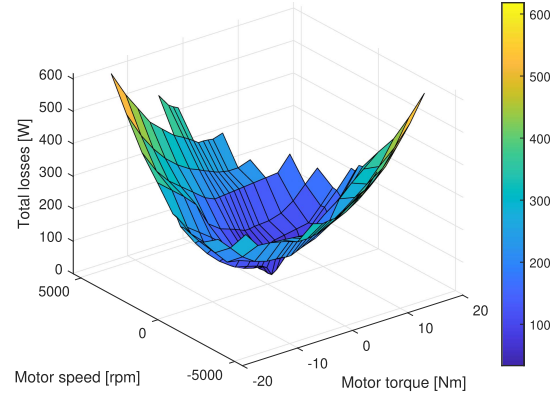
Fig. 17. Power losses in the PTO motor and driver (from measurements). (a) Total losses. (b) Mechanical losses. (c) Electrical losses utilized to parameterize the Simscape-Electrical motor and driver block. Surface colors correlate with vertical axes.

where $\tau_{\text{lab}}, \omega, V_{\text{bus}}, I_{\text{batt}}$, and I_{dl} are measured in electrical subsystem tests. The variable τ_{lab} is the torque applied by an external laboratory electric motor during the bench tests. Fig. 17(b) shows the mechanical friction losses described by (16) and Fig. 17(c) illustrates the electrical losses obtained from (18), which have been utilized to parameterize the Simscape-Electrical motor and driver block.
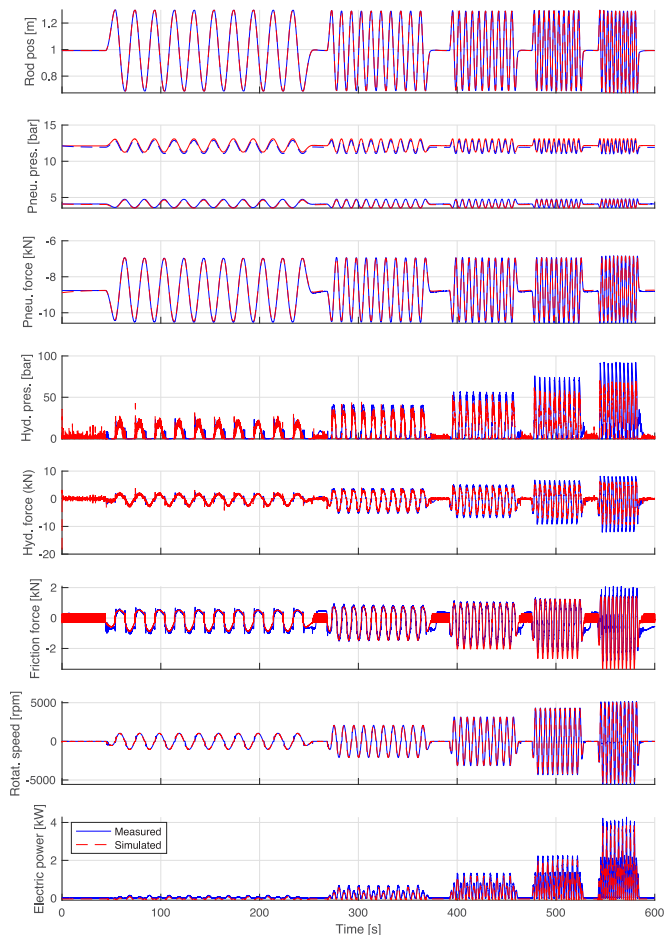
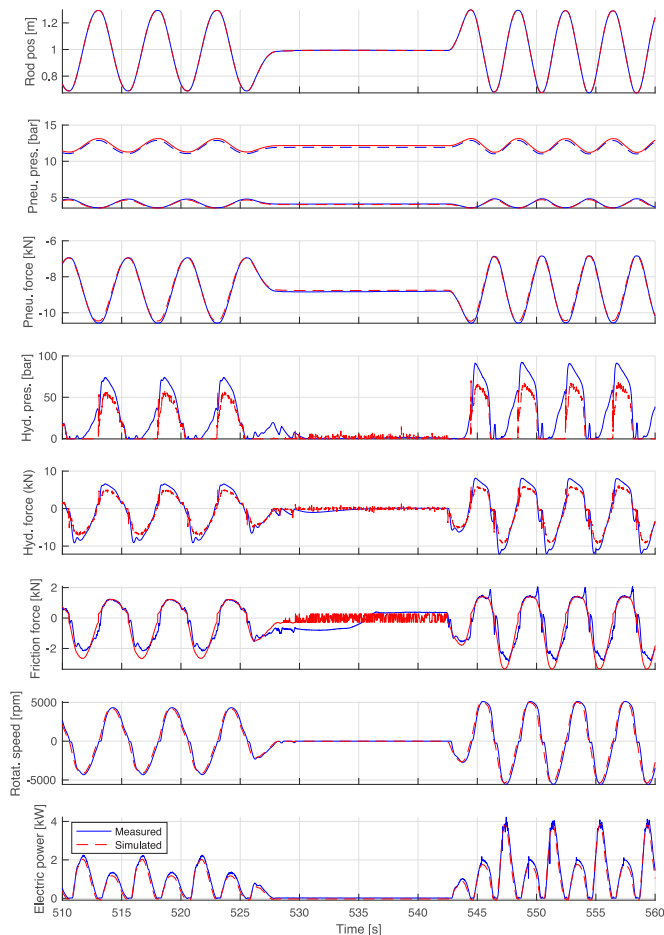Fig. 18.   Validation results with measured rod velocity used to drive numerical simulation.

Fig. 19.   Validation results with measured rod velocity used to drive numerical simulation shown for a reduced time period to enhance detail.

Electric batteries are components based on distributed electrochemical reactions, occurring in the electrodes and electrolyte. The complex inner mechanisms of a battery exhibit an interdependency between variables, such as temperature distribution, electric charge concentration, voltage, electric current, and state of charge. Different battery models exist, characterized by various levels of complexity, accuracy, and computational cost [15], [16]. In this effort, the battery and damping load (see Section II-C) have been significantly simplified, by modeling their combined behavior as a 325-V ideal constant voltage source, where voltage dependency to load variation, SoC, temperature, internal parameters, or any other transient phenomenon is neglected.

IV. COMPLETE PTO MODEL VALIDATION

Validation tests were conducted by using the experimentally measured rod speed as an input signal to the simulations together with the target torque for the PTO electric motor. A series of five sinusoidal rod oscillations were tested. In addition, the measured hydraulic and pneumatic chamber pressures p_1, p_2, p_3, and p_4 are utilized as initial conditions in the simulations. The complete results are plotted in Fig. 18. In addition, a shorter

time period ($510 \leq t \leq 560$) is plotted in Fig. 19 to provide a more detailed comparison between the measured and simulated results.

The matching between both the individual pneumatic chamber pressures and the overall pneumatic force shows very good agreement. The simulation's prediction for the hydraulic pressures shows that less accuracy has been achieved here compared to the pneumatic pressures. However, the discrepancy is less severe when the force due to the hydraulic pressures is considered. This indicates some offsetting errors in the simulation or system identification process but the resulting hydraulic force is the important quantity for the purpose of this simulator.

Similarly, the predicted friction force from the rod is fairly accurate, although there is some low amplitude high-frequency noise in the simulated friction force during periods when the rod velocity is zero. This is due to small velocities measured experimentally and applied to the simulation, which are amplified into greater friction force fluctuations by the large algebraic curve slope around the origin of the friction model (see Fig. 12—Pane 4). Since these high-frequency fluctuations are significant only when the rod piston velocity is small, their presence is not considered particularly problematic when evaluating the PTO performance.

The ability of the numerical model to accurately predict the electrical power is considered essential in evaluating the suitability of the numerical model. The simulated electric power, which is calculated as the product of V_{bus} and I_{bus}, has very good agreement with the experimental measurements. Note that the total electrical power is shown as the sum of power being delivered to the battery and power being dissipated by the load dump. The battery voltages and currents are not shown in this comparison because the specific battery behavior has not been included in this modeling effort. Instead, the battery is modeled as a constant voltage source and without internal resistance. This eliminates the challenge of matching the simulations to the exact state of charge of the batteries during the testing, at the expense of accuracy because the converter efficiency depends weakly on the bus voltage of the system. In practice, much of the electrical power generated during the testing is dissipated by the load-dump, so these shortcomings of the model do not appear in the electrical power comparison. A planned upgrade to the system is a change from the currently used lead–acid battery to a lithium iron phosphate system. This new battery has a significantly lower internal resistance so the swing in bus voltage with power will be considerably reduced.

V. Conclusion

This article describes the implementation of a new MATLAB–Simulink–Simscape model for the MBARI-WEC PTO, a system composed of hydraulic, pneumatic, and electrical subsystems, developed to provide power to various oceanic research missions. The model has been created by utilizing both manufacturer component datasheet values and information extracted from bench tests carried out on specific subsystems in the MBARI laboratory. The model is the result of the compromise between the conflicting requirements of having an accurate model without introducing excessive complexity in the model structure, which necessarily leads to the adoption of simplifying assumptions, in exchange for better numerical efficiency.

The validation of the model is carried out by comparing the simulation results with harmonically driven experimental tests. In general, the PTO model shows good performance in replicating the main dynamics of the real system. The implemented thermodynamic air spring model exhibits an excellent ability to predict the pneumatic force originated by the nitrogen chamber pressures and in repeating the hysteresis effect measured in the bench tests. The hydraulic subsystem shows the ability to model the frequency and phase of the measured hydraulic force, even if the predicted oscillation amplitude is persistently smaller than the measured one.

In general, the quantities predicted by the electrical subsystem model have a good resemblance to the experimental data. Indeed, the electric motor rotational speed is predicted with excellent agreement and the bus current shows a good similarity; furthermore, despite the fact the battery is modeled as an ideal constant voltage source, the electric power exported to the electric bus shows good agreement.

A number of areas of possible improvement of the model have been identified, which could lead to a higher prediction accuracy, which is as follows:

1) addition of some extra hydraulic loads (such as pipe restrictions) to increase the oil pressure and consequently the force generated by the hydraulic piston;
2) more complex friction model and/or filter to address high-frequency noise present near zero speed;
3) inclusion of internal resistance and state-of-charge modeling for the battery system.

References

[1] A. Hamilton, F. Cazenave, D. Forbush, R. G. Coe, and G. Bacelli, "The MBARI-WEC: A power source for ocean sensing," *J. Ocean Eng. Mar. Energy*, vol. 7, no. 2, pp. 189–200, 2021.
[2] H. Isaksson and P. Önnheim, "High precision positioning and very low velocity control of a permanent magnet synchronous motor," Master's thesis, Ind. Elect. Eng. Automat., Lund Univ., Lund, Sweden, 2015.
[3] M. Jelali and A. Kroll, *Hydraulic Servo-Systems: Modelling, Identification and Control*, Berlin Germany: Springer, 2012.
[4] P. Chapple, *Principles of Hydraulic Systems Design*, 2nd ed. New York, NY: Fluid Mechanics Collection Momentum Press, 2014.
[5] J. Sullivan, *Fluid Power: Theory and Applications*, Englewood Cliffs, NJ, USA: Prentice-Hall, 1998.
[6] A. Akers, M. Gassman, and R. Smith, *Hydraulic Power System Analysis. Fluid Power and Control*, Boca Raton, FL, USA: CRC, 2006.
[7] S. Lee, "Development and analysis of an air spring model," *Int. J. Automot. Technol.*, vol. 11, no. 4, pp. 471–479, 2010.
[8] Y. Çengel, M. Boles, and M. Kanoglu, *Thermodynamics: An Engineering Approach*, New York, NY, USA: McGraw-Hill, 2018.
[9] M. Tuckerman, *Statistical Mechanics: Theory and Molecular Simulation*, Oxford, U.K.: OUP, 2010.
[10] S. Som, *Introduction to Heat Transfer*. New Delhi: PHI Learn., 2008.
[11] Y. Liu, J. Li, Z. Zhang, X. Hu, and W. Zhang, "Experimental comparison of five friction models on the same test-bed of the micro stick-slip motion system," *Mech. Sci.*, vol. 6, no. 1, pp. 15–28, 2015.
[12] F. Marques, P. Flores, J. P. Claro, and H. M. Lankarani, "Modeling and analysis of friction including rolling effects in multibody dynamics: A review," *Multibody Syst. Dyn.*, vol. 45, no. 2, pp. 223–244, 2019.
[13] S. Andersson, A. Söderberg, and S. Björklund, "Friction models for sliding dry, boundary and mixed lubricated contacts," *Tribol. Int.*, vol. 40, no. 4, pp. 580–587, 2007.
[14] T. Soderstrom and P. Stoica, *System Identification*. Upper Saddle River, NJ, USA: Prentice-Hall, 1989.
[15] C. Zhang, K. Li, S. Mcloone, and Z. Yang, "Battery modelling methods for electric vehicles-a review," in *Proc. IEEE Eur. Control Conf.*, 2014, pp. 2673–2678.
[16] G. Saldaña, J. I. S. Martín, I. Zamora, F. J. Asensio, and O. Oñederra, "Analysis of the current electric battery models for electric vehicle simulation," *Energies*, vol. 12, no. 14, 2019, Art. no. 2750.

Simone Giorgi received the master's degree in electronics from the Università degli Studi di Ferrara, Ferrara, Italy, in 2002, and the master's and Ph.D. degrees in renewable energy systems from Maynooth University, Maynooth, Ireland, in 2012 and 2017, respectively.

Since 2017, he has been a Renewable Energy Engineer and a Consultant with Ocean Wave Venture. His research interest focuses on the numerical modeling of wave energy devices, resource assessments, and techno-economic analyses.

Ryan G. Coe received the B.S. degree in ocean engineering and the Ph.D. degree in aerospace engineering from Virginia Tech, Blacksburg, VA, USA, in 2009 and 2013, respectively.

In 2013, he joined Sandia National Laboratories' Water Power Technologies group. His research interest focuses primarily on wave energy converters (WECs), including optimizing WEC performance through dynamics-based design and control, extreme response modeling and survival analysis, and testing large-scale WEC devices.

Dr. Coe is an Associate Editor for the *Journal of Waterway, Port, Coastal, and Ocean Engineering* and on the Editorial Board for Energies. He also serves as a Convenor for International Electrotechnical Commission on the subject of "Design requirements for marine energy systems."

Scott Jensen received the B.S. degree in computer engineering from San Jose State University, San Jose CA, in 1988.

He has been working in instrumentation development for a number of decades as an Electrical Engineer. Previously, he has developed instrumentation as space flight hardware for biomedical and atmospheric research. At Monterey Bay Aquarium Research Institute, he continues to develop oceanographic instrumentation such as an in situ robotic genetic sampling and processing system as well as power electronics spanning five orders of magnitude. His contributions to these projects span the entire project life from inception through deployment support.

Meagan M. Reasoner received the B.S. degree in mathematics from Northern Michigan University, Marquette, MI, USA, in 2005, the B.S. degree in mechanical engineering from the University of Washington, Seattle, WA, USA, in 2021, and the M.Sc. degree in renewable energy engineering from the University of Exeter, Exeter, U.K., in 2022.

They are an Energy Analyst with Regen, a nonprofit energy transformation company, Exeter. They work on a variety of projects in the field of decarbonization of the U.K. energy sector. Their main project is the Distribution Future Energy Scenarios, which numerically models different distribution network operators' electricity demands and generations to meet the U.K.'s goals for Net-Zero by 2050.

François Cazenave received the master's degree in industrial engineering at EIGSI (Ecole d'Ingénieurs en Génie des Systèmes Industriels), La Rochelle, France, in 2003, and the master's degree in marine science at Moss Landing Marine Laboratories, Moss Landing, California, in 2008.

Since 2010, he has been a Mechanical Engineer with Monterey Bay Aquarium Research Institute, Moss Landing, CA, USA. He is involved in all phases of product development, from concept to deployment in the field. He has been working on a wide range of oceanographic equipment including AUVs, ROVs, camera systems, and a wave energy converter.

Giorgio Bacelli received the master's degree from Università Politecnica delle Marche, Ancona, Italy, in 2006, and the Ph.D. degree from the National University of Ireland, Maynooth, Ireland, in 2014, both in electronic engineering.

He is currently a Senior Research Engineer with Water Power Technologies Department, Sandia National Laboratories, Albuquerque, NM, USA, where the focus of his research is on the dynamics and control of wave energy converters, power take-off design, and experimental testing.

Dr. Bacelli is a Subject Matter Expert for International Electrotechnical Commission on the subject of "Guidelines for the early stage development of wave energy converters."

Andrew Hamilton received the B.S. degree in mechanical engineering from the University of Colorado Boulder, Boulder, CO, USA, in 1991, and the Ph.D. degree in mechanical engineering from the University of California, Berkeley, Berkeley, CA, USA, in 2001.

In addition to employment with Parker-Hannifin as a Motor-Control Engineer earlier in his career, he has been a Mechanical Engineer with Monterey Bay Aquarium Research Institute, Moss Landing, CA, USA, since 2001, working in the area of energy harvesting for powering autonomous systems, deep-water mooring design, hydrodynamics of underwater vehicle, and control systems.

Dominic D. Forbush received the bachelor's, master's, and doctoral degrees in mechanical engineering from the University of Washington, Seattle, WA, USA, in 2014, 2017 and 2018, respectively, where his graduate work focused on the control of cross-flow hydrokinetic turbines.

He is currently a Senior Research and Development Engineer with Water Power Technologies Program, Sandia National Laboratories, Albuquerque, NM, USA. His research interests include control, modeling, and the development of innovative solutions for wave energy converters (WECs), particularly focusing on developing and supporting open-source WEC modeling tools, wave tank testing of WEC devices and control approaches, and the application of structured innovation techniques to the wave energy space.